Crucial role of atomic corrugation on the flat bands and energy gaps of twisted bilayer graphene at the magic angle $\theta \sim 1.08°$

Procolo Lucignano,[1,*] Dario Alfè,[2,3] Vittorio Cataudella,[3,1] Domenico Ninno,[3,1] and Giovanni Cantele[1,†]

[1]*CNR-SPIN, c/o Complesso di Monte S. Angelo, via Cinthia, 80126 Napoli, Italy*
[2]*Department of Earth Sciences and London Centre for Nanotechnology, University College London,
Gower Street, London WC1E 6BT, United Kingdom*
[3]*Dipartimento di Fisica "Ettore Pancini," Università degli Studi di Napoli "Federico II,"
Complesso di Monte S. Angelo, via Cinthia, 80126 Napoli, Italy*

We combine state-of-the-art large-scale first-principles calculations with a low-energy continuum model to describe the nearly flat bands of twisted bilayer graphene at the first magic angle $\theta = 1.08°$. We show that the energy width of the flat-band manifold, as well as the energy gap separating it from the valence and conduction bands, can be obtained only if the out-of-plane relaxations are fully taken into account. The results agree both qualitatively and quantitatively with recent experimental outcomes.

I. INTRODUCTION

The moiré patterns originating from the commensurate rotation of two graphene layers with respect to each other have revealed, at small twist angles θ, that the Dirac cone picture breaks down [1–3]. Twisted bilayer graphene (TBG) at the magic angle $\theta \sim 1.08°$ shows almost flat bands (FBs) at the Fermi energy, with a measured bandwidth as small as ~ 10 meV. The FB manifold can host up to four electrons above the Fermi energy and four holes below it and is separated by an energy gap of ~ 50 meV from both higher- and lower-energy bands. When an external gate tunes the system chemical potential within these gaps, a clear band insulating phase appears. A second, unexpected insulating phase shows up at half filling of the FB manifold, both on the electron side and on the hole side (± 2 electrons with respect to charge neutrality). After electrostatic doping, achieved by gating the structure, unconventional superconductivity, with a 1.7 K critical temperature, appears in a strong pairing regime, with a phase diagram very similar to that of the underdoped cuprates. The latter two features are attributed to enhanced electron-electron or electron-phonon interaction within the FBs, respectively, and are currently under study [4,5].

This remarkable scenario reveals how the twist angle can be used as a further degree of freedom [6,7] to combine two-dimensional materials exhibiting vertical stacking to implement desired properties [8–11]. The twisted lattice geometry gives rise to topological properties of TBG [12–14], in contrast to conventional topological materials [15], where topological properties are mostly due to spin-orbit interactions [16,17] and Brillouin zone topology.

In this paper we focus on the band insulating phase, which requires an accurate description of the single-electron properties determining the band structure of the TBG. These electronic properties have been addressed mostly by adopting continuum effective models, focusing only on low-energy states [18–23], tight binding [24–29], or calculations using time-dependent Schrödinger approaches [30,31]. The point is that the unit cell, at the first magic angle $\theta = 1.08°$, contains 11 164 atoms, and this makes it impossible to perform a full many-body calculation (details of the lattice geometry and the reciprocal space can be found in Appendix A). Moreover, even a full description of the system in the framework of *ab initio* density functional theory (DFT), including atomic relaxations, remains challenging (the corresponding supercell is described by a hexagonal lattice with an in-plane lattice parameter of ~ 120 Å). To date, there are very few first-principles calculations [12,28] on TBG at small twist angles. For example, in Ref. [28] the energy bands obtained from DFT calculations carried out on the unrelaxed structure are reported. However, the *ab initio* results at the magic angle $\theta \sim 1.08°$ show no gap between the FB manifold and the closest lower band, although a band set consistent with the experimental outcomes is reproduced at a larger angle, $\theta = 1.30°$, corresponding to a smaller unit cell (7804 atoms, in contrast to 11 164 at the first magic angle). On the other hand, since the experimental uncertainty over the measured angle in Ref. [1] is of the order of $\Delta\theta \sim 0.01°$–$0.02°$, a thorough theoretical description at $1.08°$ is demanding.

In this paper we present a fully *ab initio* DFT calculation of the electronic structure of TBG at $\theta = 1.08°$ showing that a band structure consistent with that measured in Ref. [1] is obtained provided that the out-of-plane atomic relaxations are fully taken into account. In particular, the occurrence of energy gaps between the FBs and the lower- and higher-energy bands emerges as a direct consequence of the corrugation due to the out-of-plane displacements.

Such a result is strictly related to the nature of the FBs close to the Fermi energy: indeed, we can infer that the appearance of these bands is the result of the interlayer van der Waals

*procolo.lucignano@spin.cnr.it
†giovanni.cantele@spin.cnr.it

(vdW) interaction, whose effect can be tuned by controlling the twist angle. The out-of-plane relaxation of the atomic positions obviously modifies the strength of the interaction, as we are going to discuss in the following.

The paper is organized as follows. In Sec. II we describe the *ab initio* calculation with particular attention to the geometric optimization of the superlattice. In Sec. III we introduce the low-energy effective continuum model of Refs. [18–23] and specialize it to describe our optimized structures. In Sec. IV we show our numerical results. In Sec. V we summarize our findings. Appendixes A, B, and C describe the details of the geometrical structure, of the DFT *ab initio* calculation, and of the low-energy continuum model, respectively.

II. GEOMETRIC OPTIMIZATION

Although previous studies have pointed out that the atomic corrugation due to interplane vdW interaction might have relevant effects on the band structure and on the effective point symmetries [29,32–34], they were mainly based on molecular dynamics and classical interatomic potentials [26,35,36], which, as such, can give only a partial answer to the problem posed.

Here DFT calculations, using the rev-vdw-DF2 exchange-correlation functional [37], have been carried out using the Vienna Ab initio Simulation Package (VASP) [38]. The atomic positions have been fully optimized, as detailed in Appendix B. The calculation required from 2880 (distributed over 80 nodes) up to 5760 physical cores (distributed over 160 nodes) of a Cray XC-40 machine over a period of about 30 days.

The outcome of the geometry optimization is depicted in Fig. 1, where we use a color map to show the out-of-plane
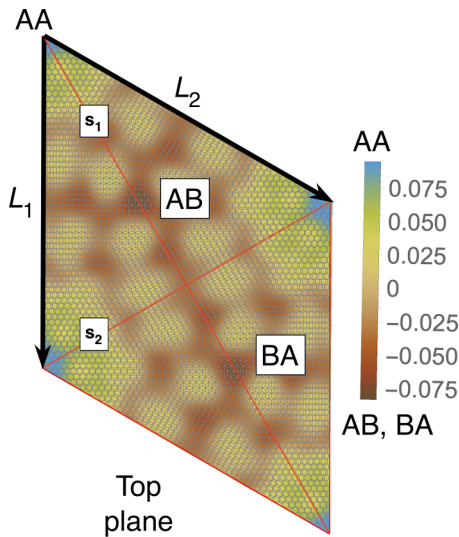

FIG. 1. Color map of the top layer relaxation (color labels are expressed in angstroms and correspond to the difference $\Delta z = z - z_{\text{avg}}$ between the actual z coordinate and the average coordinate z_{avg} in the top plane) as obtained from first-principles DFT calculations. AA and AB/BA stacking regions are highlighted, along with the supercell sides $\mathbf{L}_1$, $\mathbf{L}_2$.

deformation of the top layer. Inspection shows that atomic relaxation tends to increase the interplane distance in correspondence to the AA stacking regions and to decrease it in the AB regions. Out-of-plane displacements are modulated on the length scale, intermediate between the moiré and the graphene periodicities, and seem to be in agreement with the emergent D_6 symmetry described in Ref. [29]. As we will show in the following, these geometric properties have severe consequences on the electronic band structure of the system. Details of the optimized structure are shown in Fig. 2. In the top panels we illustrate the characteristics of the TBG top plane: in particular, in Figs. 2(a) and 2(b) we show the corrugation profile respectively along the line $\mathbf{s}_1 = s(\mathbf{L}_1 + \mathbf{L}_2)$, $0 \leqslant s \leqslant 1$ and the line $\mathbf{s}_2 = \mathbf{L}_1 + s(\mathbf{L}_2 - \mathbf{L}_1)$, $0 \leqslant s \leqslant 1$ (both shown in Fig. 1). In Fig. 2(c) we show a histogram representing the atomic population binned according to the z coordinate of the atoms. The same features are shown in Figs. 2(d)–2(f) for the the TBG bottom plane. The corrugations show clear oscillations along the lines $\mathbf{s}_1$ and $\mathbf{s}_2$; however, a simple analytical expression interpolating between the atomic position is not easily accessible due to the large harmonic content of the oscillatory behavior. The peaks of the histograms define an average z coordinate for the top plane ($z_{\text{avg}}^{\text{top}}$) and for the bottom plane ($z_{\text{avg}}^{\text{bottom}}$). Their difference defines the average interlayer spacing $z_{\text{avg}}^{\text{top}} - z_{\text{avg}}^{\text{bottom}} = 3.408$ Å that is halfway between the equilibrium distances of 3.31 and 3.496 Å between consecutive planes in graphite with AB Bernal and AA stackings, respectively (both calculated using the same rev-vdw-DF2 exchange-correlation functional). Within each plane, the atomic displacements occur within an interval of about 0.2 Å (± 0.1 Å with respect to the average z in each plane).

III. EFFECTIVE CONTINUUM MODEL

To increase the understanding of the *ab initio* results, we also describe a continuum model generalizing the model proposed in Refs. [18,21–23], providing an effective low-energy band structure which shows remarkable agreement with the DFT calculation. Our results can be viewed as an accurate single-particle description of TBG at the first magic angle and used as a starting point for a full many-body calculation taking into account electronic correlations. In the following we briefly summarize the model, referring to Refs. [19,22,23] for further details. At small twist angles, the moiré period L_M is much longer than the lattice constant a. The superlattice mini Brillouin zone (MBZ) extends over a tiny area of the graphene BZ, and it is a hexagon whose vertices are the two Dirac points $K_\xi^{(1)}$ and $K_\xi^{(2)}$ of the two layers after rotation (compare small and large hexagons in Fig. 7), where $\xi = \pm 1$ is the valley index. Close to these points the single-layer graphene spectrum can be safely assumed to be linear, and a low-energy (long-wavelength) Hamiltonian of each layer $l = 1, 2$ can be used:

$$H_\xi^{(l)}(\mathbf{k}) = -\hbar v_F \{R[(-1)^{l+1}\theta/2](\mathbf{k} - \mathbf{K}_\xi)\} \cdot (\xi\sigma_x, \sigma_y), \quad (1)$$

where $R(\theta)$ is a two-dimensional matrix describing the rotation by θ, $\hbar v_F/a = 2.1354$ eV and σ_x, σ_y are Pauli's matrices. In the following we neglect the intervalley mixing because of the huge distance between the two graphene valleys on the
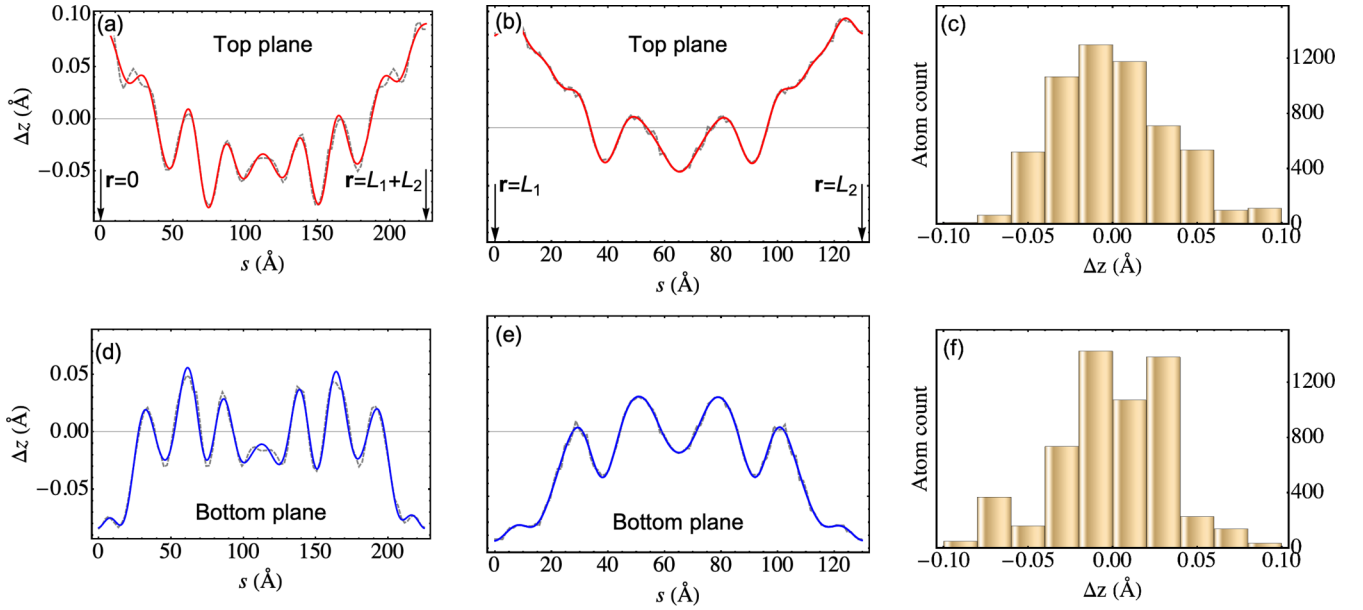
FIG. 2. Analysis of the atomic corrugation. In the top panels we illustrate the characteristics of the top plane: (a) corrugation profile along the line $\mathbf{s}_1 = s(\mathbf{L}_1 + \mathbf{L}_2)$, $0 \leqslant s \leqslant 1$, shown in Fig. 1. $\Delta z = z - z_{\mathrm{avg}}$ is the deviation of the z coordinate with respect to the average z of the top plane z_{avg}. Thin dashed lines correspond to the real atomic z coordinate, while solid colored lines are interpolating functions. (b) Corrugation profile along the line $\mathbf{s}_2 = \mathbf{L}_1 + s(\mathbf{L}_2 - \mathbf{L}_1)$, $0 \leqslant s \leqslant 1$, shown in Fig. 1. (c) The histogram represents the atomic population binned according to the Δz. (d)–(f) The same features as in (a)–(c), respectively, for the bottom plane, with Δz built according to the average z coordinate of the bottom plane.

MBZ scale. Hence, each valley can be studied separately. In the presence of interlayer interaction the bilayer system can be described by the matrix Hamiltonian

$$H_\xi(\mathbf{k}) = \begin{pmatrix} H_\xi^{(1)}(\mathbf{k}) & U_\xi^\dagger \\ U_\xi & H_\xi^{(2)}(\mathbf{k}) \end{pmatrix}. \qquad (2)$$

The off-diagonal coupling terms are expressed in terms of overlap integrals u, u' (see Appendix C). The parameters u and u' are calculated in Ref. [23] at $\mathbf{k} = \mathbf{K}_\xi^{(l)}$ and kept constant when calculating the band structure for all the k points in the MBZ. As the MBZ is a small hexagon of side $|\mathbf{K}_\xi^{(1)} - \mathbf{K}_\xi^{(2)}| \sim |\mathbf{K}_\xi^{(l)}|\theta$, it seems to be a reasonable approximation, particularly at small twist angles. In our calculations, in order to give a minimal model capable of describing (at least) the low-energy properties of the *ab initio* band structure, we do not calculate u, u' but use them as fitting parameters. In the following we will show that the fitted parameters are relatively close to (but quantitatively different from) those obtained performing the hopping integrals shown in Appendix C. Such a discrepancy can be ascribed to the fact that a low-energy effective model obtained expanding a tight-binding Hamiltonian around the $\mathbf{K}_\xi$ point does not entail all the complexity of the full *ab initio* approach but, nevertheless, can constitute a relevant tool to get closer and closer to the desired solution, with an accurate choice of the model parameters.

The wave function is calculated as a linear superposition of plane waves of momentum $\mathbf{G}$, where $\mathbf{G}$ are reciprocal lattice vectors. The $\mathbf{G}$ point expansion extends, in principle, over the full (infinite) set of $\mathbf{G}$ vectors. However, for numerical purposes this set has to be truncated. We choose a cutoff radius G_{cut} and keep only the $\mathbf{G}$ vectors inside the sphere

of radius G_{cut}. It turns out that the number N_G of required vectors to converge the lowest-energy states is rather small. The low-energy continuum Hamiltonian matrix has the dimension $D = 4N_G$, and $N_G = 19$ (as in the example reported in Fig. 7) allows for a good convergence in an energy shell of a few hundred meV around the Fermi energy, whereas full convergence, i.e., band energies converged within less than 1 meV, is achieved with $N_G = 37$.

IV. RESULTS AND DISCUSSION

In Fig. 3 we represent the band structure calculated in the absence of structural relaxation. The blue dots are the outcome of a DFT *ab initio* calculation, while the solid curves are obtained by diagonalizing the continuum model in the two valleys: $\xi = \pm 1$. The parameters $u = u' = 0.1085$ eV are obtained after the fitting procedure on the *ab initio* points. The results show reasonable agreement between these two approaches. Here we discuss some relevant features emerging from our numerical calculations.

First of all, we may notice that the FB has a dispersion of $\sim$20 meV (calculated *ab initio*), which is almost twice the one measured in the experiment of Ref. [2]. Another relevant issue is that the unrelaxed *ab initio* calculation is not able to reproduce the gap between the FB and the first excited bands (both on the electron side and on the hole side) that are responsible for the band insulating phases. Our calculation performed adopting the low-energy continuum model shows good agreement with the *ab initio* calculation and reproduces all its relevant features. A few discrepancies show up when zooming in on the very fine details of the FB (see the right panel of Fig. 3), which are not relevant as they do not change
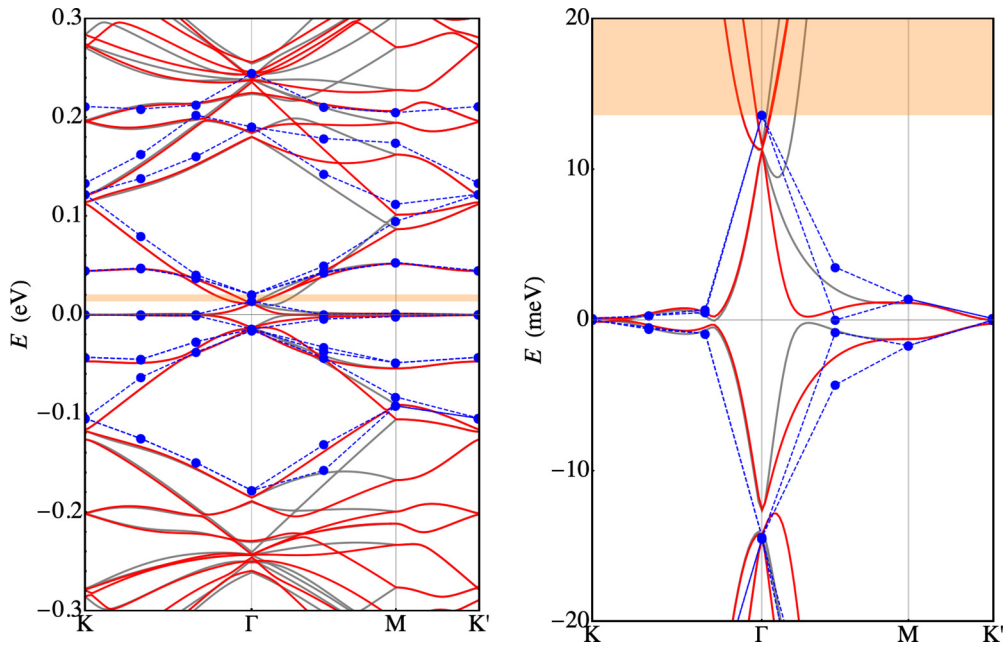
FIG. 3. Left: Unrelaxed band structure along the K-Γ-M-K' line as derived from the continuum model (solid red and gray lines represent bands deriving from the $\xi = 1$ and $\xi = -1$ valleys, respectively). Blue dots are the results of the *ab initio* calculation. Right: Zoom around the Fermi energy of the left panel, highlighting the nearly FB. Zero energy corresponds to the Fermi level. The orange shaded regions correspond to the energy ranges of the DFT gaps. Note the absence of any gap between the four flat bands and the low-energy part of the spectrum.

the way the data compare with experiments. However, these results point in the direction that it is not possible to interpret experimental data using an unrelaxed structure.

Relaxation of the structure drastically changes the scenario, with substantial agreement with the experiments. Plots of the relaxed band structures are shown in Fig. 4. The parameters $u = 0.0761$ eV, $u' = 0.1031$ eV are again obtained by fitting the *ab initio* band structure. The FB now extends for $\sim$12 meV around the Fermi level (calculations performed with larger supercells with z axis $= 12$ and 14 Å show that
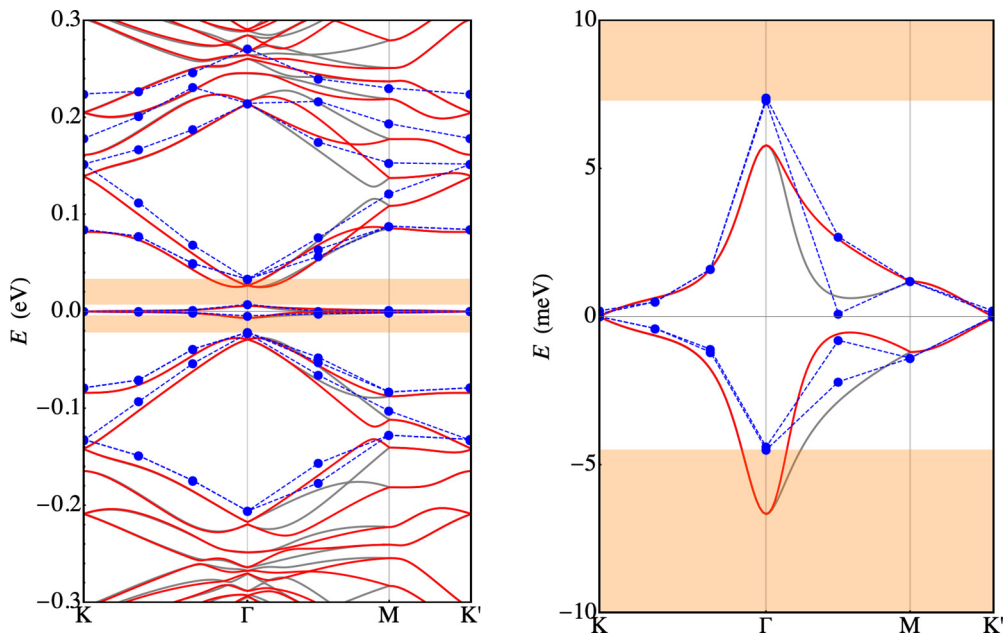

FIG. 4. Left: Relaxed band structure along the K-Γ-M-K' line as derived from the continuum model (solid red and gray lines represent bands deriving from the $\xi = 1$ and $\xi = -1$ valleys, respectively). Blue dots are the results of the *ab initio* calculation. Right: Zoom around the Fermi energy of the left panel, highlighting the nearly FB. Zero energy corresponds to the Fermi level. The orange shaded regions correspond to the energy ranges of the DFT gaps. Note the opening of the gap between the four flat bands and the low-energy part of the spectrum, caused by the relaxation of the atomic coordinates.
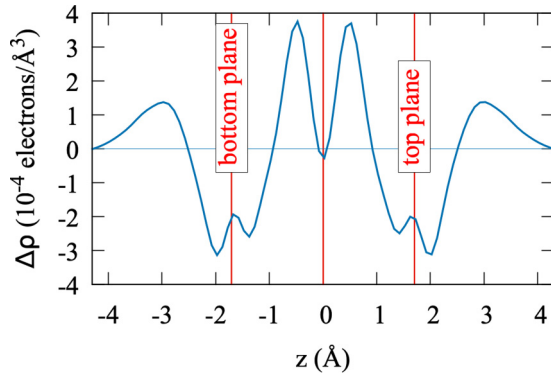
FIG. 5. Computed DFT charge transfer: Positive (negative) values correspond to filling (depletion) of electron charge.

this number is subject to an error of approximately 3 meV). That bandwidth is in good agreement with the one measured in experiments ($\leqslant 10$ meV; see Ref. [1]). It is separated by a gap of 26 meV (16 meV) from the highest occupied (lowest unoccupied) bands, which should be compared with the thermal activation gap of ~ 40 meV measured in experiments. Such discrepancy is not much larger than the convergence error in the DFT calculations. It is clear that the vdW interplane interactions, despite being weak, play a crucial role in determining the details of the TBG at the meV level. This is confirmed by the computed charge transfer, shown in Fig. 5. It is defined as $\Delta\rho(\mathbf{r}) = \rho(\mathbf{r}) - \rho_1\mathbf{r}) - \rho_2(\mathbf{r})$, where $\rho(\mathbf{r})$ is the total charge density of TBG, whereas $\rho_i(\mathbf{r})$, $i = 1, 2$, are the charge densities of the top and bottom planes, respectively, calculated by removing the other plane from the supercell at frozen atomic positions. Figure 5 shows the average charge transfer over planes orthogonal to the z axis. It turns out that an electronic charge depletion shows up within each plane, and most of the charge is redistributed in the interplane region.

V. CONCLUSIONS

To summarize, our calculations can finally give a clear explanation of some of the most striking features of the electronic structure of TBG at the first magic angle $\theta = 1.08°$. In particular, the extension of the FBs and the presence of band gaps separating them from excited states on both the negative- and positive-energy sides can be explained successfully in terms of atomic out-of-plane displacements. By allowing a full *ab initio* structural optimization, a non-negligible atomic corrugation shows up in both the graphene layers. As expected from simple electrostatic arguments, the interlayer distance gets larger (smaller) at AA (AB/BA) stacking regions, with a maximum (minimum) distance of ~ 3.68 Å (3.28 Å). Such a corrugation is a direct consequence of the interplay between vdW interaction and twisting of the graphene layers. It implies a decrease of the FB bandwidth of ~ 4 meV and induces gaps between the FB and the closer bands, in good agreement with the experimental findings. Our *ab initio* results can also be interpreted in terms of a simple continuum model in which interplane hopping potentials have been used as fitting parameters. This simple model reproduces with reasonable accuracy the electronic structure and could pave the way for further

investigations to better describe also the other relevant phases of the TBG at a small twist angle, i.e., the superconducting and correlated insulating ones.

APPENDIX A: LATTICE GEOMETRY AND RECIPROCAL SPACE

Let $\mathbf{a}_i$, $i = 1, 2$, be the vectors defining the graphene primitive cell, where $\mathbf{a}_1 = a(1, 0)$, $\mathbf{a}_2 = a(1/2, \sqrt{3}/2)$, and $a \sim 0.2456$ nm is the lattice constant. The corresponding reciprocal lattice vectors are $\mathbf{b}_1 = (2\pi/a)(1, -1/\sqrt{3})$ and $\mathbf{b}_2 = (2\pi/a)(0, 2/\sqrt{3})$. In the absence of geometric relaxation, let us consider, as a starting point, the unrotated bilayer with perfect AA stacking (each C atom in the first layer lying exactly on top of a C atom in the second layer). Choosing a pair of stacked C atoms, each belonging to one of the layers, the twisted bilayer at angle θ can be obtained by rotating the first and second layers around the axis passing through these atoms (which indeed are fixed points of the rotation) by $-\theta/2$ and $\theta/2$, respectively. After rotation, the Bravais direct lattices of the first and second layers are described by the vectors $\mathbf{a}_i^{(l)} = R(\mp\theta/2)\mathbf{a}_i$, and the reciprocal lattice is described by the vectors $\mathbf{b}_i^{(l)} = R(\mp\theta/2)\mathbf{b}_i$, where $l = 1, 2$ identifies the layer and $R(\theta)$ is a two-dimensional matrix describing the rotation by θ. For an arbitrary rotation angle, the resulting structure shows a moiré pattern but is aperiodic and cannot be described through a Bravais lattice because the periods of the two layers are, in general, incommensurate. However, periodic structures can be achieved when θ is the angle between two lattice vectors $\mathbf{d}_1 = n\mathbf{a}_1 + m\mathbf{a}_2$ and $\mathbf{d}_2 = m\mathbf{a}_1 + n\mathbf{a}_2$, with (n, m) being an arbitrary pair of integers. The points at $\mathbf{d}_1$ and $\mathbf{d}_2$ merge after the rotation of the two planes, and the lattice vectors of the moiré supercell are thus given by $\mathbf{L}_1 = n\mathbf{a}_1^{(1)} + m\mathbf{a}_2^{(1)} = m\mathbf{a}_1^{(2)} + n\mathbf{a}_2^{(2)}$ and $\mathbf{L}_2 = R(\pi/3)\mathbf{L}_1$. The rotation angle can be expressed in terms of the integers n, m as $2\cos\theta = (m^2 + n^2 + 4mn)/(m^2 + n^2 + mn)$. The magic angle $\theta = 1.08°$ corresponds to $(n, m) = (31, 30)$, with the number of atoms in the unit cell given by $N = 4 |(\mathbf{L}_1 \times \mathbf{L}_2)|/|(\mathbf{a}_1 \times \mathbf{a}_2)| = 11\,164$. As $n = m + 1$, the lattice constant $L = |\mathbf{L}_1| = |\mathbf{L}_2| = a|m - n|/[2\sin(\theta/2)] \sim 12.78$ nm is coincident in this case with the moiré pattern period $L_M = a/[2\sin(\theta/2)]$ [22].

Figure 6 shows the atomic structure of the TBG at $\theta = 1.08°$ (four unit supercells are shown). The moiré patterns originating from regions with different stacking are highlighted: AA and AB/BA, with AB (BA) corresponding to the stacking of a C atom in the top (bottom) layer and the center of a hexagon in the other layer.
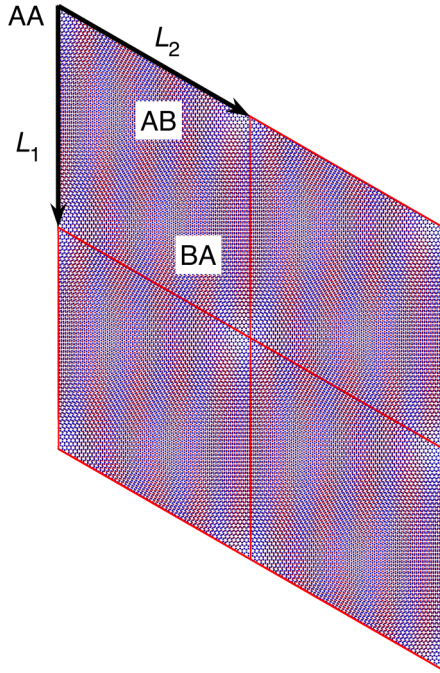
FIG. 6. The moiré pattern originating from the superposition of two graphene layers after rotation by the commensurate angle 1.08°. AA and AB/BA stacking regions are highlighted, along with the supercell sides $\mathbf{L}_1, \mathbf{L}_2$. Blue (red) dots represent atoms in the top (bottom) plane. Four unit supercells are shown.

The reciprocal lattice vectors for the moiré pattern are obtained as $\mathbf{G}_i = \mathbf{b}_i^{(1)} - \mathbf{b}_i^{(2)}$ ($i = 1, 2$). The resulting mini Brillouin zone (MBZ) is shown as a dark hexagon in the center of Fig. 7. It should be noticed that the Brillouin zones (BZs) of the two graphene layers are rotated with respect to each other by the same angle as the graphene layers themselves,
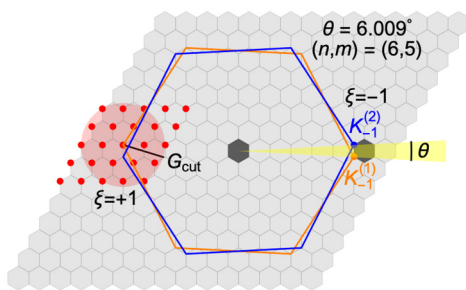

FIG. 7. The reciprocal lattice of the moiré supercell. The central mini Brillouin zone is highlighted with a dark hexagon and periodically replicated (light gray hexagons). The rotation angle is $\theta = 6.009°$, corresponding to $(n, m) = (6, 5)$ (a larger angle than the first magic angle is considered to produce a clearer representation of the MBZ). $\xi = \pm 1$ denotes the valley in the BZs of the single layers, and $K_\xi^{(l)}$ is the K point of layer $l = 1, 2$ at valley ξ. The bigger (blue and orange) hexagons represent the BZs of the layers after rotation, and the rotation angle θ is highlighted. Red dots correspond to a uniform grid of G vectors of the supercell reciprocal lattice. Only G vectors up to a given distance from a K point (red shaded circle) are included in the expansion required in the continuum model (see text).

as shown in Fig. 7 (blue and orange bigger hexagons). As such, each graphene layer $l = 1, 2$ has its Dirac points at $\mathbf{K}_\xi^{(l)} = -\xi(2\mathbf{b}_1^{(l)} + \mathbf{b}_2^{(l)})/3$, where $\xi = \pm 1$ labels the valley index. For example, in Fig. 7 we also show the K points at the $\xi = -1$ valley for both layers. It turns out that $K_\xi^{(1)} - K_\xi^{(2)}$ coincides with one of the sides of the MBZ.

APPENDIX B: DFT *AB INITIO* CALCULATIONS

Density functional theory calculations, using the rev-vdw-DF2 exchange-correlation functional [37], were carried out using the Vienna Ab initio Simulation Package (VASP) [38]. We used a projector augmented-wave potential [39,40] for carbon with the $2p$ orbitals in valence and the $1s$ orbitals frozen in the core. The single-particle Bloch waves were expanded with a plane wave basis set, using a cutoff energy of 400 eV. Sampling the BZ for the self-consistent (SCF) calculations was restricted at the Γ point. Single-particle energies at other points in the BZ were obtained with non-SCF calculations. Because of the size of the simulation cell, we could compute only one k point at a time, and the reported single-particle energies were therefore referred to the Fermi energy computed as the energy at the K point. The size of the supercell in the direction orthogonal to the layers (z axis) was initially fixed at 10 Å, corresponding to about 6.5-Å vacuum space, introduced to prevent periodic replicas of the TBG supercell from interacting with each other. Full relaxation of the atomic positions was carried out until the residual forces were smaller than 0.002 eV/Å. Additional calculations were repeated using supercells with a z axis of 12 and 14 Å. A small residual (maximum) relaxation of less than 0.002 Å was observed as the z axis was increased to 12 Å, but no further relaxation was detectable with the largest 14-Å vacuum space. The initial relaxation was carried out using 2880 physical cores distributed over 80 nodes of a Cray XC-40 machine over a period of about 30 days. Calculations with 14-Å vacuum required 5760 cores on 160 nodes to accommodate the extra memory requirements. All symmetries were turned off.

APPENDIX C: EFFECTIVE CONTINUUM MODEL

In the presence of interlayer interaction the bilayer system can be described by the matrix Hamiltonian

$$H_\xi(\mathbf{k}) = \begin{pmatrix} H_\xi^{(1)}(\mathbf{k}) & U_\xi^\dagger \\ U_\xi & H_\xi^{(2)}(\mathbf{k}) \end{pmatrix}. \tag{C1}$$

The interlayer Hamiltonian is

$$\begin{aligned} U_\xi &= \begin{pmatrix} U_{A_2 A_1} & U_{A_2 B_1} \\ U_{B_2 A_1} & U_{B_2 B_1} \end{pmatrix} \\ &= \begin{pmatrix} u & u' \\ u' & u \end{pmatrix} + \begin{pmatrix} u & u'\omega^{-\xi} \\ u'\omega^{\xi} & u \end{pmatrix} e^{i\mathbf{G}_1 \cdot \mathbf{r}} \\ &+ \begin{pmatrix} u & u'\omega^{\xi} \\ u'\omega^{-\xi} & u \end{pmatrix} e^{i(\mathbf{G}_1 + \mathbf{G}_2) \cdot \mathbf{r}}, \end{aligned} \tag{C2}$$

with $\omega = e^{i2\pi/3}$. It couples each $\mathbf{k}$ point of the first layer to a $\mathbf{k}'$ point of the second layer according to the selection rules $\mathbf{k}' = \mathbf{k}, \mathbf{k} + \mathbf{G}_1, \mathbf{k} + \mathbf{G}_1 + \mathbf{G}_2$. The coefficients u, u' are given in

Ref. [23]:

$$u(\mathbf{k}) = -\frac{1}{S_0} \int t[\mathbf{R} + d(\mathbf{R})\mathbf{e}_z] e^{-i\mathbf{k}\cdot\mathbf{R}} d^2\mathbf{R},$$
$$u'(\mathbf{k}) = -\frac{1}{S_0} \int t[\mathbf{R} + d(\mathbf{R} - \boldsymbol{\tau}_1)\mathbf{e}_z] e^{-i\mathbf{k}\cdot\mathbf{R}} d^2\mathbf{R}, \quad \text{(C3)}$$

where $S_0 = \sqrt{3}/2a^2$ is the unit cell area of the pristine graphene and $t(\mathbf{R})$ is the transfer integral between two sites at distance $\mathbf{R}$, originating from the Slater-Koster tight-binding parametrization for p_z carbon atoms:

$$t(R) = -V_{pp\pi} \left[1 - \left(\frac{\mathbf{R} \cdot \hat{\mathbf{z}}}{R}\right)^2 \right] - V_{pp\sigma} \left(\frac{\mathbf{R} \cdot \hat{\mathbf{z}}}{R}\right)^2,$$
$$V_{pp\pi} = V_{pp\pi}^0 e^{(R-a_0)/r_0}, \quad V_{pp\sigma} = V_{pp\sigma}^0 e^{(R-d_0)/r_0}. \quad \text{(C4)}$$

Here $r_0 = 0.184a$ is the decay length of the transfer integral, $a_0 = a/\sqrt{3}$ is the first-neighbor distance in graphene, and $d_0 = 0.335$ nm is the intralayer distance, chosen in agreement with that of graphite. $V_{pp\pi}^0 = -2.7$ eV and $V_{pp\sigma}^0 = 0.48$ eV are the in-plane and out-of-plane nearest-neighbor hopping

energy from Ref. [22]. We seek for solutions of the kind

$$\begin{pmatrix} \psi_{n\mathbf{k}}^{A_1}(\mathbf{r}) \\ \psi_{n\mathbf{k}}^{B_1}(\mathbf{r}) \\ \psi_{n\mathbf{k}}^{A_2}(\mathbf{r}) \\ \psi_{n\mathbf{k}}^{B_2}(\mathbf{r}) \end{pmatrix} = \sum_{\mathbf{G}} \begin{pmatrix} c_{n\mathbf{k}}^{A_1}(\mathbf{G}) \\ c_{n\mathbf{k}}^{B_1}(\mathbf{G}) \\ c_{n\mathbf{k}}^{A_2}(\mathbf{G}) \\ c_{n\mathbf{k}}^{B_2}(\mathbf{G}) \end{pmatrix} e^{i(\mathbf{k}+\mathbf{G})\cdot\mathbf{r}}. \quad \text{(C5)}$$

The $\mathbf{G}$ point expansion extends, in principle, over the full (infinite) set of $\mathbf{G}$ vectors. However, for numerical purposes this set has to be truncated. We choose a cutoff radius G_{cut} and keep only the $\mathbf{G}$ vectors inside the sphere of radius G_{cut}. This is schematically shown in Fig. 7, where the shaded circle of radius G_{cut} includes the subset of $\mathbf{G}$ vectors, represented by the red dots. It turns out that the number N_G of vectors to converge the lowest-energy states is rather small. The low-energy continuum Hamiltonian matrix has the dimension $D = 4N_G$, and $N_G = 19$ (as in the example reported in Fig. 7) allows for good convergence in an energy shell of few hundred meV around the Fermi energy, whereas full convergence, i.e., band energies converged within less than 1 meV, is achieved with $N_G = 37$.

---

[1] Y. Cao, V. Fatemi, A. Demir, S. Fang, S. L. Tomarken, J. Y. Luo, J. D. Sanchez-Yamagishi, K. Watanabe, T. Taniguchi, E. Kaxiras, R. C. Ashoori, and P. Jarillo-Herrero, Nature (London) **556**, 80 (2018).

[2] Y. Cao, V. Fatemi, S. Fang, K. Watanabe, T. Taniguchi, E. Kaxiras, and P. Jarillo-Herrero, Nature (London) **556**, 43 (2018).

[3] E. Codecido, Q. Wang, R. Koester, S. Che, H. Tian, R. Lv, S. Tran, K. Watanabe, T. Taniguchi, F. Zhang, M. Bockrath, and C. N. Lau, arXiv:1902.05151.

[4] Y. W. Choi and H. J. Choi, Phys. Rev. B **98**, 241412(R) (2018).

[5] A. O. Sboychakov, A. V. Rozhkov, A. L. Rakhmanov, and F. Nori, arXiv:1807.08190.

[6] R. Ribeiro-Palau, C. Zhang, K. Watanabe, T. Taniguchi, J. Hone, and C. R. Dean, Science **361**, 690 (2018).

[7] F. Conte, D. Ninno, and G. Cantele, Phys. Rev. B **99**, 155429 (2019).

[8] A. K. Geim and I. V. Grigorieva, Nature (London) **499**, 419 (2014).

[9] G. Cantele and D. Ninno, Phys. Rev. Mater. **1**, 014002 (2017).

[10] I. Borriello, G. Cantele, and D. Ninno, Nanoscale **5**, 291 (2012).

[11] G. Cantele, Y.-S. Lee, D. Ninno, and N. Marzari, Nano Lett **9**, 3425 (2009).

[12] Z. Song, Z. Wang, W. Shi, G. Li, C. Fang, and B. A. Bernevig, arXiv:1807.10676.

[13] K. Hejazi, C. Liu, H. Shapourian, X. Chen, and L. Balents, Phys. Rev. B **99**, 035111 (2019).

[14] J. Liu, J. Liu, and X. Dai, Phys. Rev. B **99**, 155415 (2019).

[15] M. Z. Hasan and C. L. Kane, Rev. Mod. Phys. **82**, 3045 (2010).

[16] D. Bercioux and P. Lucignano, Rep. Prog. Phys. **78**, 106001 (2015).

[17] P. Lucignano, R. Raimondi, and A. Tagliacozzo, Phys. Rev. B **78**, 035336 (2008).

[18] J. M. B. Lopes dos Santos, N. M. R. Peres, and A. H. Castro Neto, Phys. Rev. Lett. **99**, 256802 (2007).

[19] J. M. B. Lopes dos Santos, N. M. R. Peres, and A. H. Castro Neto, Phys. Rev. B **86**, 155449 (2012).

[20] E. J. Mele, Phys. Rev. B **81**, 161405(R) (2010).

[21] R. Bistritzer and A. H. MacDonald, Proc. Natl. Acad. Sci. USA **108**, 12233 (2011).

[22] P. Moon and M. Koshino, Phys. Rev. B **87**, 205404 (2013).

[23] M. Koshino, N. F. Q. Yuan, T. Koretsune, M. Ochi, K. Kuroki, and L. Fu, Phys. Rev. X **8**, 031087 (2018).

[24] J. Jung and A. H. MacDonald, Phys. Rev. B **87**, 195450 (2013).

[25] A. O. Sboychakov, A. L. Rakhmanov, A. V. Rozhkov, and F. Nori, Phys. Rev. B **92**, 075402 (2015).

[26] S. Fang and E. Kaxiras, Phys. Rev. B **93**, 235153 (2016).

[27] X. Lin and D. Tománek, Phys. Rev. B **98**, 081410(R) (2018).

[28] J. Kang and O. Vafek, Phys. Rev. X **8**, 031088 (2018).

[29] M. Angeli, D. Mandelli, A. Valli, A. Amaricci, M. Capone, E. Tosatti, and M. Fabrizio, Phys. Rev. B **98**, 235137 (2018).

[30] V. N. Do, H. A. Le, and D. Bercioux, Phys. Rev. B **99**, 165127 (2018).

[31] H. A. Le and V. N. Do, Phys. Rev. B **97**, 125136 (2018).

[32] K. Uchida, S. Furuya, J.-I. Iwata, and A. Oshiyama, Phys. Rev. B **90**, 155451 (2014).

[33] M. M. van Wijk, A. Schuring, M. I. Katsnelson, and A. Fasolino, 2D Mater. **2**, 034010 (2015).

[34] X. Lin, D. Liu, and D. Tománek, Phys. Rev. B **98**, 195432 (2018).

[35] F. Gargiulo and O. V. Yazyev, 2D Mater. **5**, 015019 (2018).

[36] S. K. Jain, V. Juričić, and G. T. Barkema, 2D Mater. **4**, 015018 (2016).

[37] I. Hamada, Phys. Rev. B **89**, 121103(R) (2014).

[38] G. Kresse and J. Furthmüller, Phys. Rev. B **54**, 11169 (1996).

[39] P. E. Blöchl, Phys. Rev. B **50**, 17953 (1994).

[40] G. Kresse and D. Joubert, Phys. Rev. B **59**, 1758 (1999).